

See discussions, stats, and author profiles for this publication at: <https://www.researchgate.net/publication/235901959>

# Structure, Dynamics, and Phase Behavior of Water in TiO<sub>2</sub> Nanopores

ARTICLE *in* THE JOURNAL OF PHYSICAL CHEMISTRY C · FEBRUARY 2013

Impact Factor: 4.77 · DOI: 10.1021/jp307900q

---

CITATIONS

12

---

READS

58

5 AUTHORS, INCLUDING:



Galo J A A Soler-Illia

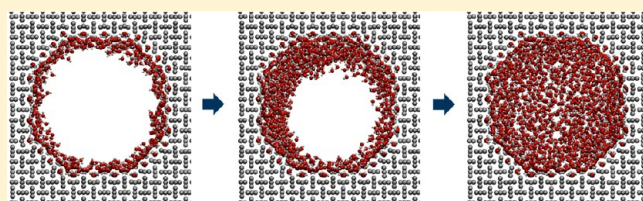
National University of General San Martín

144 PUBLICATIONS 8,178 CITATIONS

SEE PROFILE

1 **Structure, Dynamics, and Phase Behavior of Water in TiO<sub>2</sub> Nanopores**2 Estefanía González Solveyra,<sup>†</sup> Ezequiel de la Llave,<sup>†</sup> Valeria Molinero,<sup>‡</sup> Galo Soler-Illia,<sup>†,§</sup>  
3 and Damian A. Scherlis<sup>\*,†</sup>4 <sup>†</sup>Departamento de Química Inorgánica, Analítica y Química Física, Facultad de Ciencias Exactas y Naturales, Universidad de Buenos  
5 Aires, Pab II, Ciudad Universitaria, Buenos Aires C1428EHA, Argentina6 <sup>‡</sup>Department of Chemistry, University of Utah, 315 South 1400 East, Salt Lake City, Utah 84112-0850, United States7 <sup>§</sup>Gerencia Química Comisión Nacional de Energía Atómica, Centro Atómico Constituyentes, Av. Gral Paz 1499, San Martín,  
8 B1650KNA Buenos Aires, Argentina9 **S** Supporting Information

**ABSTRACT:** Mesoporous titania is a highly studied material due to its energy and environment-related applications, which depend on its tailored surface and electronic properties. Understanding the behavior of water in titania pores is a central issue for practical purposes in photocatalysis, solar cells, bone implants, or optical sensors. In particular, the mechanisms of capillary condensation of water in titania mesopores and the organization and mobility of water as a function of pore filling fraction are not yet known. In this work, molecular dynamics simulations of water confined in TiO<sub>2</sub>-rutile pores of diameters 1.3, 2.8, and 5.1 nm were carried out at various water contents. Water density and diffusion coefficients were obtained as a function of the distance from the surface. The proximity to the interface affects density and diffusivity within a distance of around 10 Å from the walls, beyond which all properties tend to converge. The densities of the confined liquid in the 2.8 and the 5.1 nm pores decrease, respectively, 7% and 4% with respect to bulk water. This decrease causes the water translational mobility in the center of the 2.8 nm pore to be appreciably larger than in bulk. Capillary condensation takes place in equilibrium for a filling of 71% in the 2.8 nm pore and in conditions of high supersaturation in the 5.1 nm pore, at a filling of 65%. In the former case, the surface density increases uniformly with filling until condensation, whereas in the larger nanopore, a cluster of water molecules develops on a localized spot on the surface for fillings just below the transition. No phase transition is detected in the smaller pore. For all the systems studied, the first monolayer of water is strongly immobilized on the interface, thus reducing the accessible or effective diameter of the pore by around 0.6 nm. As a consequence, the behavior of water in these pores turns out to be comparable to its behavior in less hydrophilic pores of smaller size.

30 **■ INTRODUCTION**

31 In recent years, a remarkable proficiency was achieved in both  
32 the synthesis and the physical characterization of mesoporous  
33 inorganic materials.<sup>1–10</sup> Impelled by the fundamental interest in  
34 chemistry and physics under confinement and their applica-  
35 tions, the synthetic community has gained an extraordinary  
36 expertise in controlling the size and shape of nanoscopic  
37 cavities in inorganic solids. A wide variety of materials has been  
38 used in this context, inorganic oxides being among the most  
39 explored.<sup>3–6,8,10</sup> As a consequence, the behavior of water  
40 confined in hydrophilic porous networks has received plenty of  
41 attention, resulting in a large number of studies addressing  
42 adsorption and capillary condensation,<sup>11–16</sup> and turning, more  
43 recently, to the solid–liquid transition,<sup>17–20</sup> the structure,<sup>20,21</sup>  
44 transport,<sup>22</sup> and dynamics<sup>23–25</sup> of H<sub>2</sub>O, with the assistance of  
45 techniques such as nuclear magnetic resonance (NMR), Raman  
46 scattering, and differential scanning calorimetry. Much of this  
47 work has been conducted on silica matrixes of moderate  
48 hydrophilicity with pores in the range 1 to 10 nm  
49 diameter.<sup>12–25</sup> The shapes of adsorption–desorption isotherms  
50 and their temperature dependence was described in many of

these studies,<sup>12–16</sup> including the characterization of the  
hysteresis cycle, which was found to disappear for diameters  
below 1.7 nm at room temperature.<sup>13</sup> The filling of silica pores  
of 3.3 and 8 nm was investigated through <sup>1</sup>H NMR  
spectroscopy by Grünberg and co-workers.<sup>21</sup> Two filling  
mechanisms were proposed: in the narrower pores, capillary  
condensation was preceded by monolayer coverage. In the  
wider pores, instead, a radial thickening involving several layers  
took place before capillary condensation was observed.<sup>21</sup> More  
recent NMR relaxometry measurements in pores of 4.5 nm by  
Steiner and collaborators<sup>25</sup> led to the determination of the  
correlation times associated with the inter- and intramolecular  
relaxation rates of water within the pores. On the basis of these  
data, the authors introduced a classification of the water  
molecules in three types: an adsorbed layer of slow molecules, a  
second more mobile layer with correlation times 5-fold lower

Received: April 6, 2012

Revised: January 15, 2013

(around 0.1 ns), and a third group of essentially free water with correlation times in the order of 1 ps.<sup>25</sup>

Computer simulations provide a powerful way to explore the behavior of molecules in nanospaces. Many examples can be found where Monte Carlo and molecular dynamics approaches have been applied to describe the adsorption of simple compounds in nanopores.<sup>26–38</sup> The effect of different water–substrate interaction strengths on the phase states of water was investigated by Brovchenko et al. using molecular dynamics and Gibbs ensemble Monte Carlo methods in cylindrical and slit-like nanopores with featureless surfaces.<sup>29,30</sup> These authors observed bulk-like liquid–vapor phase transitions in hydrophobic pores, whereas they identified three additional types of phase coexistence in more hydrophilic systems and classified them as first layering transition, second layering transition, and prewetting. Liquid coexistence with an adsorbed bilayer was typically seen for the most hydrophilic pores.<sup>30</sup> Debenedetti and co-workers analyzed the diffusion of water dwelling between planar surfaces as a function of temperature,<sup>33</sup> hydrophilicity,<sup>34</sup> and confinement.<sup>35</sup> Interestingly, they found that the water diffusion coefficient in the region next to the interface becomes maximum for an intermediate hydrophilicity. This is a consequence of the fact that a hydrophobic surface induces an ice-like structure in the interfacial water molecules, while a highly polar interface leads to strong interactions, which tend to immobilize the adjacent water layers.<sup>34</sup> In another study, Wei et al. compared the diffusion of water in TiO<sub>2</sub> and graphite slit pores in the 0.8–2.0 nm range, showing that the H<sub>2</sub>O mobility is highly restrained in the former and that the diffusion coefficient is strongly affected by the separation between pore walls.<sup>36</sup> In recent work, we have shown that, for water in moderately hydrophilic pores with adsorption energies comparable to those found in MCM-41 and FSM-16 silica pores, there is an onset filling at which capillary condensation is unleashed, forming a condensed liquid phase, which coexists with a low-density phase consisting of water adsorbed on the pore walls.<sup>37</sup> Above this water content, further addition of molecules to the system does not alter the densities of the two phases in equilibrium but causes an increase in the amount of the condensed liquid phase. We found that, in 3 nm pores, the surface density just before the point of capillary condensation exceeds by a factor of 2 of the density in equilibrium after condensation, i.e., the phase transition occurs in conditions of supersaturation.<sup>37</sup> The dependence of this behavior on pore radius and hydrophilicity was the subject of a subsequent study.<sup>38</sup> This overshooting of the surface density, which can be related to the hysteresis cycle in adsorption–desorption isotherms, was not observed in the narrowest pore of 1.5 nm,<sup>37,38</sup> neither in systems of moderate hydrophilicity. Our simulations revealed two filling mechanisms for pores in the range 3.0–4.0 nm, depending on the water–surface affinity: (i) a gradual filling in equilibrium for surfaces of moderate hydrophobicity, with an affinity for the surface slightly below the one of water with itself and (ii) an out of equilibrium transition associated with adsorption hysteresis for hydrophilic nanopores.<sup>38</sup>

Following the direction of the experiments, much of the computational work has been focused on water within silica pores, using atomistic potentials. Shirono and Daiguji performed canonical ensemble molecular dynamics and grand canonical Monte Carlo (GCMC) simulations in silica pores in the range 1–3 nm, to examine the phase behavior of H<sub>2</sub>O.<sup>39</sup> Three kinds of phases were characterized, depending on pore

size and filling, consisting of (i) a submonolayer coverage with water molecules exclusively solvating the silanol groups, (ii) a condensed monolayer, and (iii) a completely water-filled pore. In addition, they determined that the translational mobility of water in the first adsorption layer was much smaller than the bulk value as a result of the strong interaction with the surface groups, in agreement with quasi-elastic neutron scattering studies confirming that the translational diffusion coefficient of confined water decreases as the pore diameter is diminished.<sup>24</sup> Malani et al. reported GCMC computations comparing the confining effects of silica and mica flat surfaces.<sup>40</sup> The density, the dipole moment distributions, and the pair correlation functions of water were analyzed, with an emphasis on the effect that the K<sup>+</sup> ions at the mica interface exert in structuring the hydration layer. Gallo and co-authors discussed the structure and dynamical properties of supercooled water and the glass transition in cylindrical silica pores on the basis of molecular dynamics simulations.<sup>41–43</sup> A more recent molecular dynamics and GCMC study by Milischuk and Ladanyi examined the structure and dynamics of water at room temperature in amorphous silica nanopores of 2, 3, and 4 nm diameters.<sup>44</sup> Among the main findings, they identified two distinctive interfacial water layers, beyond which the water density became homogeneous, reaching 90% of the bulk value. The parallel and radial components of the diffusion coefficients were found to be very similar for a given layer (or a given distance to the surface). The translational mobility in the center of the pore turned out to be higher than in bulk, which the authors attributed to the lower density in the core region.<sup>44</sup>

In spite of the extended use of titania in mesoporous assemblies with applications in photocatalysis, solar cells, or bone implants,<sup>3–5,45,46</sup> the behavior of water confined in these pores has not been subject to a comparable microscopic analysis derived from molecular simulations. The interaction of water with TiO<sub>2</sub> surfaces is around three times stronger than with silica, and therefore, important differences are likely to arise between the structure and the dynamics of water confined in each one of these materials. The TiO<sub>2</sub>–H<sub>2</sub>O flat interface has been thoroughly studied from first-principles.<sup>47–53</sup> Density functional theory (DFT) calculations performed by different research groups, including ours, have pointed out that, for water multilayers, molecular adsorption predominates on undefective anatase (101)<sup>49,52,53</sup> and rutile (110) faces.<sup>50–53</sup> Only in recent years atomistic force-fields have been derived for the interaction of water with TiO<sub>2</sub> surfaces,<sup>54,55</sup> allowing for large scale molecular dynamics simulations of flat interfaces and nanoparticles in contact with aqueous solutions.<sup>55–57</sup> To the best of our knowledge, the present study is first to investigate the properties of water in cylindrical titania nanopores using molecular simulations. We provide an account of the structure, the translational and rotational mobility, and the liquid–vapor equilibrium of H<sub>2</sub>O in fully and partially filled TiO<sub>2</sub> cylindrical pores of different sizes. Our purpose is to achieve a microscopic understanding of water confined in highly hydrophilic nanoconfined geometries, which is critical in applications such as Grätzel solar cells, selective membranes, photocatalysts, and biomaterials, and can in turn be compared to the abundant literature on water in silica and other solids.

## ■ PORE MODELS AND COMPUTATIONAL METHODS

**Model Systems and Fillings.** We constructed cylindrical channels of diameters 1.3, 2.8, and 5.1 nm and lengths 10.6, 7.1, and 7.1 nm, respectively. In each case, the central portion of a

bulk crystalline rutile was drilled out, rendering cylindrical pores with the pore axis parallel to the [001] direction, which will be referred to as the  $z$ -direction. The structures and crystallographic axes are shown in the Supporting Information. A criterion of maximum saturation for the cations was adopted to generate the surface, exposing only six- and five-coordinate titanium atoms and three- and two-coordinate oxygen atoms, as found in rutile (110). Water dissociation at the interface was neglected, which seems a reasonable assumption for the (110) face.<sup>53</sup> In particular, our own quantum-mechanical calculations on steps and kinks of the  $\text{TiO}_2$  surface partially reproducing the wall structure in cylindrical pore models suggest that molecular absorption is also favored on these sites (see Supporting Information or ref 58). Simulations were carried out with periodic boundary conditions. The pores were filled with different numbers of water molecules to obtain various filling fractions. The 100% is defined for a pore fully filled with liquid water in equilibrium at the point of capillary condensation. The density of such a liquid can be extracted from a canonical simulation where the condensed (or high density) phase coexists with the low density phase: as will be shown in the Filling Mechanisms and Phase Transition section, this is the case for fillings larger than 71% in the 2.8 nm pore or larger than 65% in the 5.1 nm pore. In the condition of coexistence, both phases exhibit their corresponding equilibrium densities at the transition point at 300 K. In the smaller pore, however, the situation of two phases in equilibrium is never reached. A possible way to obtain the equilibrium density in this case would be to consider a large reservoir filled with water and connected to the pore. However, because of the slow diffusion, simulation times required to equilibrate the pore plus reservoir system turned out to be beyond the reach of atomistic simulations. Therefore, the filling in the 1.3 nm pore is simply defined with respect to the density of bulk water at 300 K (0.997 g/cm<sup>3</sup>), this is, the quantity of water at 100% filling is equal to 1.3 nm  $\times$   $\pi$   $\times$   $L$   $\times$  0.997 g/cm<sup>3</sup>, with  $L$  the length of the pore.

**Force Field.** The  $\text{H}_2\text{O}$  molecules were represented with the SPC/E potential,<sup>59</sup> with its internal degrees of freedom restrained through the SHAKE algorithm.<sup>60</sup> The metal–oxide and the oxide–water interactions were modeled with the force-field proposed by Bandura and Kubicki,<sup>54</sup> which combines Buckingham, Coulomb, Morse, and dispersive-repulsive terms, and is an extension of the potential devised for bulk titania by Matsui and Akaogi.<sup>61</sup> This model yields a molecular adsorption energy for water of 25.2 kcal/mol and a bond length of 2.20 Å, which compare well with the values of 21.7 kcal/mol and 2.17 Å predicted by DFT.<sup>54</sup> Given the curvature of the interface, the atomic charges of the surface atoms had to be slightly rescaled to preserve the electroneutrality, without affecting the energetics or structure.

**Simulation Methods.** Atomistic molecular dynamics simulations of water in the  $\text{TiO}_2$  pores were performed in the canonical ensemble using LAMMPS.<sup>62,63</sup> The particle–particle–mesh (PPPM) method was used to compute long-range Coulombic interactions.<sup>64</sup> All runs were subject to an initial equilibration stage of 1 ns at high temperature, followed by a cooling ramp to 300 K, after which statistical sampling was prolonged for around 5 ns. This protocol produces in all cases a uniform distribution, totally decorrelated from the initial structure, ensuring that no bias exists toward any particular configuration. Independence of the results from the initial configuration and from the equilibration procedure

has been verified in various cases. Details on these tests are given in the Supporting Information. Ti and O atoms of the pore surface were allowed to move during the dynamics. More internal  $\text{TiO}_2$  atoms, starting from the second layer, were kept fixed to save computational time. Configurations were saved every 1 ps. Equations of motion were integrated using time-steps of 1 fs, and the Nosè–Hoover thermostat was applied to control the temperature. The VMD program was used for visual analysis of the data.<sup>65</sup>

**Surface Density.** The surface density  $\Gamma$  is defined as the (average) number of molecules per unit area, and it is computed by counting the number of molecules on a slice of the pore, divided by the surface area  $A$  of such slice. If the length of the slice (along the axial direction) is  $L$ , then  $A = 2\pi RL$ , with  $R$  the radius of the pore. In the presence of a single, axially homogeneous phase,  $\Gamma$  is proportional to the filling fraction, as stated in eq 2 of ref 37. To obtain the surface density profiles of water along the pores, histograms of the number of water molecules in each pore were constructed every  $\sim 0.5$  Å along the pore axis and averaged over  $\sim 4$  ns trajectories equilibrated at the indicated water contents. The histograms were then normalized by the area of the cylinder slice to yield the surface density profiles of water along the pores normalized per unit of pore area.

**Radial and Axial Density Profiles.** Local densities along the radial and axial directions within the pores were computed for each system as in ref 37, considering the position of the oxygen atoms of the water molecules.

**Translational Dynamics.** The diffusion coefficients were computed locally on the basis of mean-square displacements, as proposed by Lounnas and co-authors in ref :

$$D_{\text{local}} = \frac{1}{6(t_2 - t_1)} (\langle |r(t_2) - r(t_0)|^2 \rangle - |r(t_1) - r(t_0)|^2 ) \quad (1)$$

where  $r(t)$  is the position of a water molecule at time  $t$ , and the averages on the quantity  $|r(t) - r(0)|$  run over time origins and over all molecules situated within the corresponding region at  $t = 0$ . Following refs 66 and 67, the time intervals  $t_1$  and  $t_2$ , of 1 and 2 ps, respectively, are chosen long enough to allow for the diffusional regime to be reached, but short enough to prevent the molecule from traveling too far from its original layer.

**Rotational Dynamics.** We computed the correlation functions of the vectorial dipole moments  $\mu_i(t)$  of the water molecules

$$C_\mu(t) = \frac{\langle \hat{\mu}_i(t) \cdot \hat{\mu}_i(0) \rangle}{\langle \hat{\mu}_i(0) \cdot \hat{\mu}_i(0) \rangle} \quad (2)$$

to investigate the orientational motions of liquid water confined in the nanopores.

## RESULTS AND DISCUSSION

**Structure.** We equilibrated water at various contents inside titania pores of diameters 1.3, 2.8, and 5.1 nm. We first focus on the structure of water in the 1.3 nm nanopore as a function of pore filling percentage. As explained above, this filling percentage is defined with respect to a system totally filled with water, with the density of the bulk liquid at the center of the pore ( $r < 2.0$  Å). Radial density profiles at different filling fractions in the smaller pore are depicted in Figure 1. Upon the addition of water molecules, we observe the formation of a layered structure, with no sign of the development of a



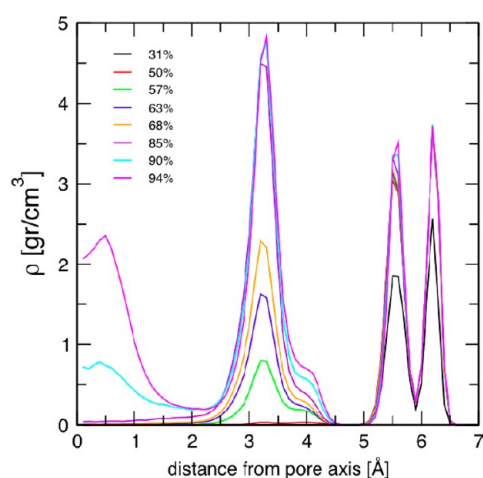


**Figure 1.** Radial density profile of water in the 1.3 nm titania pore at different water fillings. The titanium atoms at the surface occur at two distances of the pore axis, resulting in a split external peak for water directly attached to the Ti at the surface.

to a less hydrophilic pore of less than 1 nm, for which capillary 352 condensation is not observed.<sup>68</sup> On the basis of adsorption 353 experiments, Naono and Hakuman have established a diameter 354 between 0.9 and 1.1 nm for the closure point of the hysteresis 355 loop and the disappearance of capillary condensation of water 356 in TiO<sub>2</sub> and SiO<sub>2</sub> nanopores.<sup>68</sup> The high hydrophilicity of 357 titania imposes more stringent conditions to remove all the 358 water from the interface. Therefore, unless drying was 359 performed at very high temperature (this was not informed), 360 it is not unlikely that the pore surface was partially hydrated 361 even at the lowest pressures examined, in which case the 362 estimated sizes would be effective sizes. 363

The radial density of H<sub>2</sub>O in the 2.8 and 5.1 nm pores with a 364 filling of 100% is exhibited in Figure 3. The filling percentage of 365 the two large pores is defined with respect to the equilibrium 366 density of the confined liquid at 300 K at the point of capillary 367 condensation, as described in the methodological section. The 368 general pattern is the same for both nanopores: we can see two 369 external groups of peaks separated by around 3 Å, resembling 370 those of Figure 1, and corresponding to the first and second 371 water monolayers. Then there is a smooth peak revealing a 372 much less structured third layer 3 Å away from the second one. 373 In the next section, we show that the water in this third layer 374 has already reached around 75% of the maximum possible 375 mobility inside the pore. Beyond this layer, the density is 376 practically homogeneous, and the mobility of H<sub>2</sub>O is 377 comparable to the one it has in bulk (see below). In general, 378 the profiles found for these pores are reminiscent of the density 379 profiles for water on planar TiO<sub>2</sub> rutile surfaces, studied via 380 molecular dynamics simulations by Wei and collaborators in 381 confined geometries<sup>36</sup> and in the solid–liquid interface by 382 Předota and other authors.<sup>56,69,70</sup> In both the curved and the 383 planar interfaces, water molecules are organized in two well 384 discernible layers, plus a much smoother third one, beyond 385 which the density becomes uniform. Two major differences, 386 however, are readily apparent: in the case of the planar surface, 387 the peaks are not split, and the separation between the water 388 layers is significantly smaller (their approximate positions are 389 2.1, 3.9, and 4.9 Å from the interface<sup>36,69,70</sup>). Also, each water 390 molecule of the second layer is hydrogen-bonded to a bridge 391 oxygen atom of the oxide.<sup>70</sup> The analysis of the number of H- 392 bonds with the surface in all three pores is summarized in Table 393 2. It can be seen that almost 50% of the molecules in the 394 second layer are prevented from forming hydrogen bonds with 395 the bridging oxygen atoms, compared to what was reported for 396 planar rutile (110). These differences can be attributed to the 397 curvature of the pore surface, more restrictive to accommodate 398 the adjacent multilayers, and its rugosity, the water layers attach 399 to the Ti binding sites, which are not equidistant from the pore 400 center, and so the peaks corresponding to the various water 401 layers split up. A figure exhibiting typical structures of the water 402 layers in the different pores can be found in the Supporting 403 Information. Interestingly, the fraction of molecules in the 404 second layer forming bonds with the surface is about the same 405 for all three pores. While the expected behavior is an increase in 406 the number of H-bonds when the curvature is decreased, the 407 present result may suggest that such an increase is not gradual 408 but occurs in a series of steps, reflecting a discontinuous 409 reorganization of the layer as the diameter of the pore becomes 410 larger. In other words, only when the curvature is reduced 411 below a certain threshold, the layer can adopt a different 412 configuration that allows for the formation of more than 1/2 of 413 hydrogen bond per molecule. To prove this conjecture, pores 414

311 homogeneous, liquid-like phase. At around 50% filling, the first 312 adsorbed monolayer becomes complete. The two peaks in 313 Figure 1 appearing at around 6 Å and separated by less than 1 314 Å, the furthest from the center, belong to the first monolayer. 315 The contour of the crystalline interface resembles a polygon 316 rather than a perfect circumference, and so the penta- 317 coordinate Ti<sup>V</sup> atoms of the surface are not equidistant from 318 the pore center. As a consequence, the oxygen atoms directly 319 attached to these titanium sites give two peaks in the radial 320 density profile. This may be appreciated in Figure 2a. The first 321 layer of water is tightly bound to the titania surface. In fact, 322 within the times spanned by our simulations, this layer behaves 323 as a frozen shell, which practically shows no exchange of 324 molecules with the outer layers. This is reflected by very low 325 diffusion coefficients and high residence times, as shown in 326 Table 1 and Figure 6, which will be further discussed in the 327 Dynamics section. For a filling close to 85%, the second 328 monolayer develops completely. It can be noticed in Figure 2 329 that the growth of this second monolayer is not homogeneous 330 along the pore axis but proceeds through the nucleation of 331 water aggregates (see the snapshot for a filling of 63%). This 332 phenomenon has been checked to be independent from the 333 thermalization procedure or the starting configuration (see 334 Supporting Information for further details). It is not observed 335 during the growth of the first layer because the strong 336 interaction with the surface controls the addition of new 337 molecules until all high-affinity sites are saturated. The space 338 left after completion of the second monolayer in the 1.3 nm 339 pore allows for the accommodation of a single row of additional 340 water molecules in an almost 1D arrangement, giving rise to the 341 first peak in the radial density profile in Figure 1. Therefore, the 342 filling of this pore takes place gradually, with no sign of capillary 343 condensation or advent of a second phase. This result is at 344 variance with experimental<sup>11,13</sup> and computational<sup>37,38</sup> evidence 345 of capillary condensation reported for pores of around 2 nm 346 with a less hydrophilic character. This apparent contradiction 347 may be rationalized noticing that the quasi-solid water shell at 348 the TiO<sub>2</sub> interface is diminishing the effective radius of the pore 349 in nearly 3 Å, and so, the space accessible to more mobile water 350 is in the range of the micropore size. In other words, we may 351 expect the behavior of titania pores of 1.3 nm to be comparable

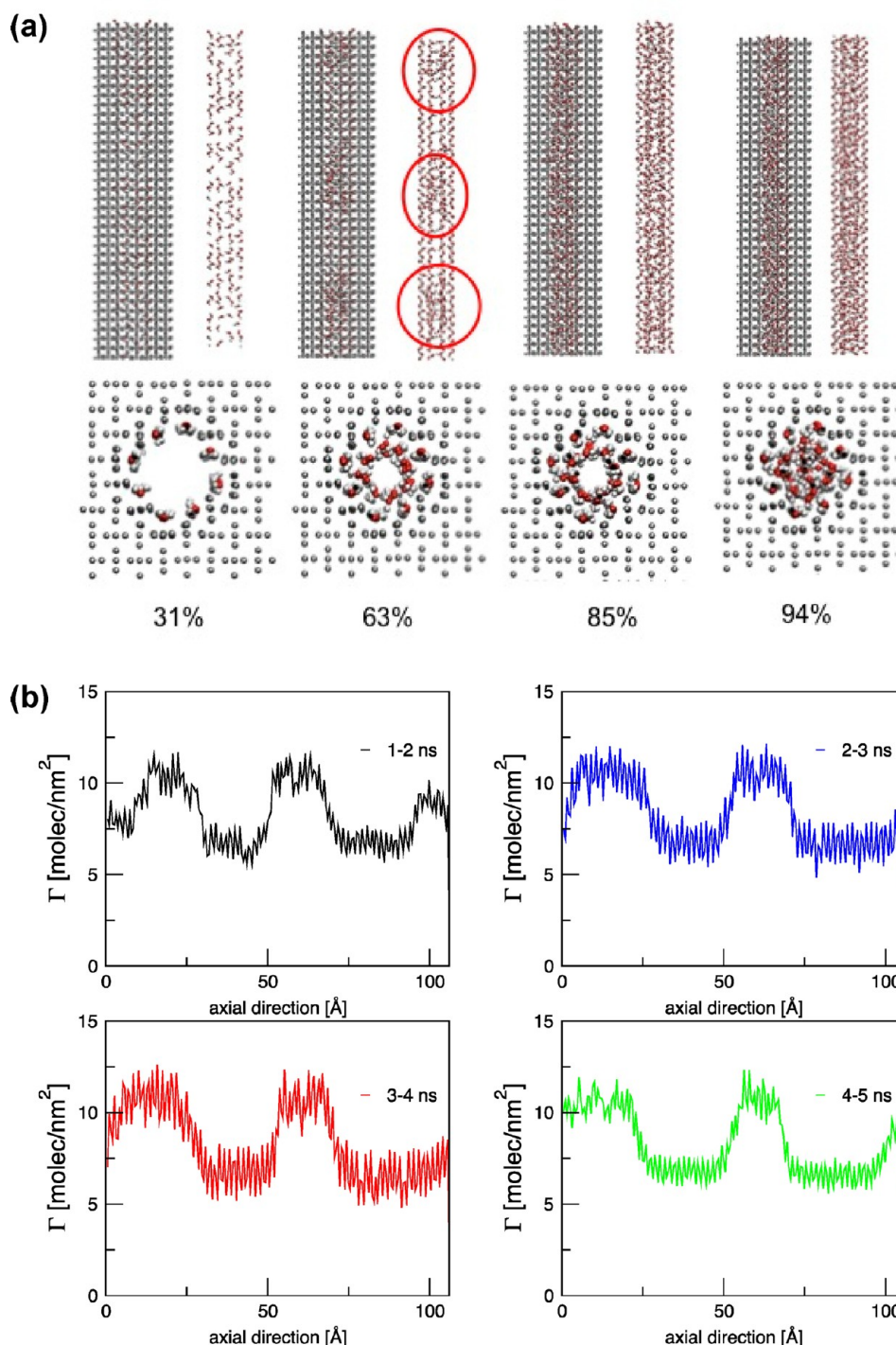


**Figure 2.** (a) Snapshots taken from the molecular dynamics of the 1.3 nm titania pore at various water fillings. Red corresponds to oxygen atoms, white to hydrogen atoms, and gray to the pore atoms. The layers grow with the increasing water content until the pore is completely filled, without the apparent formation of a plug. The circles indicate regions of higher water density that develop at intermediate water content. (b) Axial density profiles in the 1.3 nm pore at 63% filling, when the second layer appears, averaged along different time windows, showing the clustering of water molecules. The fine, oscillatory structure appearing in all profiles, does not arise from incomplete sampling, but from the immobilized water of the first hydration layer.

of large diameters or surfaces of smooth curvatures should be tested. Figure 4 depicts the number of water–water hydrogen bonds as a function of the distance to the interface. In general terms, it is seen that this number converges to the bulk value very rapidly for all three pores. Already for the second layer, the number of H-bonds is almost the same as in bulk, although the mobility of the molecules in this layer is still quite low. A similar

recovery of the hydrogen bond network has been observed for water in silica pores.<sup>44</sup>

Comparison with the density profiles reported for silica pores of similar diameters<sup>39,44,71</sup> throw the following two main differences with respect to the present results for titania: (i) the number of layers and (ii) the density maxima and minima at the interface. Studies of water in cylindrical silica pores in the range

**Table 1. Diffusion Coefficients ( $10^{-5}$  cm<sup>2</sup>/s) of Water Corresponding to Maximum Filling for Each Pore, Calculated Locally with eq 1 for the Different Regions Listed in Table 3<sup>a</sup>**

region	$d = 1.3$ nm		$d = 2.8$ nm		$d = 5.1$ nm	
	$D$	$D_z$	$D$	$D_z$	$D$	$D_z$
1	0.005	0.008	0.013	0.011	0.015	0.011
2	0.222	0.324	0.721	0.932	0.554	0.657
3	0.783	1.145	1.962	2.200	1.862	2.106
4			2.456	2.633	2.510	2.663
5			2.595	2.775	2.765	2.859
6					2.883	2.939

<sup>a</sup> $D$ , global diffusion coefficient.  $D_z$ , axial component of the diffusion coefficient. The bulk value from our MD simulations of the SPC/E water model at 300 K and 1.0 g/cm<sup>3</sup> is  $2.56 \times 10^{-5}$  cm<sup>2</sup>/s.

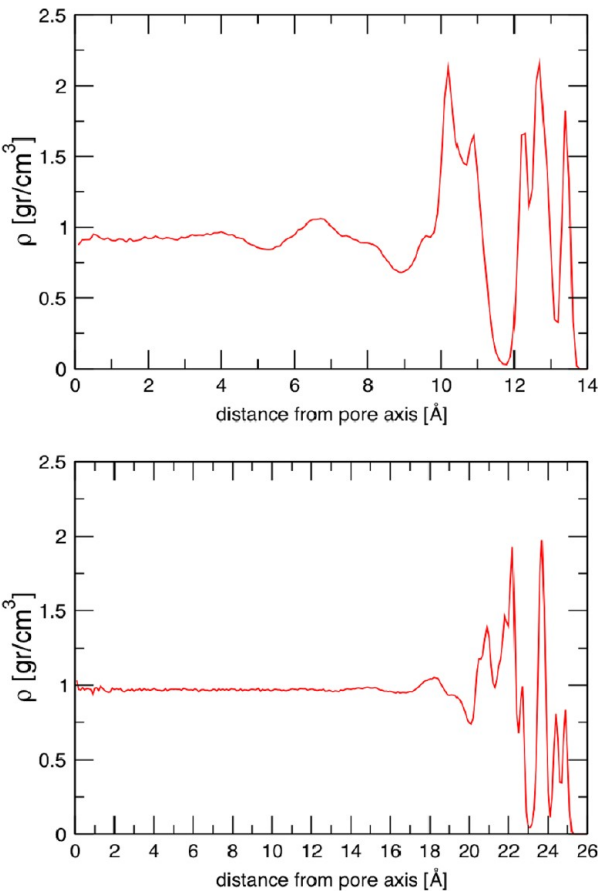


**Figure 3.** Radial density profile for the 2.8 nm (upper panel) and the 5.1 nm (lower panel) pores at 100% filling.

**Table 2. Number of Hydrogen Bonds between the Surface Bridging O Atoms and Water Molecules in the First and Second Layers, Normalized by the Total Number of Water Molecules in Each Layer<sup>a</sup>**

$d$ (nm)	$\langle \text{HB 1st layer}/n_{\text{H}_2\text{O}} \rangle$	$\langle \text{HB 2nd layer}/n_{\text{H}_2\text{O}} \rangle$
1.3	1.104	0.508
2.8	0.875	0.517
5.1	0.891	0.502

<sup>a</sup>Hydrogen-bonds defined as in ref 79.

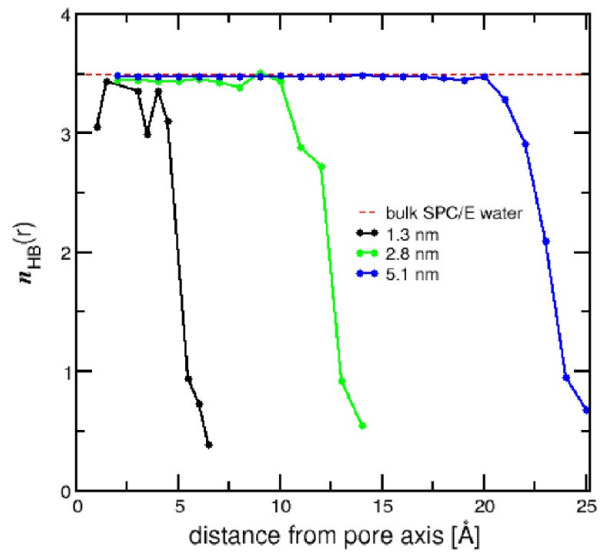


**Figure 4.** Hydrogen bonds between water molecules in the different pores, as a function of the distance to the pore axis.

1–4 nm show one<sup>39,71</sup> or, at most, two peaks<sup>44</sup> in the radial density profile. The difference between the various published results is possibly arising from the model pore shape (which usually is not a perfect cylinder) and the degree of hydroxylation of the surface. Aside from this, the density near the interface typically varies between 0.8 and 1.4 g/cm<sup>3</sup>. In contrast, the radial density profile in TiO<sub>2</sub> pores exhibits two sharp peaks plus a smooth third one, which reach maximum values close to 2 g/cm<sup>3</sup> and fall almost to zero in the interlayer space. In particular, the first two layers are more compact than in silica, where the average width is close to 4 Å. All these features evince the significantly more ordered nature of the hydration layers of titania pores, compared to silica, due to the much higher hydrophilicity of the former.

**Dynamics.** The data presented in this section correspond to the maximum filling for all 3 pores, unless explicitly noted; at the end of the section, we examine the relationship between diffusivity and filling. The mobility observed for the water molecules is strongly dependent on their proximity to the surface. For this reason, the diffusion coefficients presented in Table 1 have been calculated locally for separate radial layers according to eq 1.

For the 1.3 nm pore, three radial layers were considered, centered on each one of the three peaks appearing in Figure 1 (recall the two peaks at around 6 Å correspond to a single water layer). Region 1 encompasses a layer extending from the interface to a radius of 5 Å, region 2 from 5 to 2 Å, and region 3 from 2 Å to the center of the pore. For the 2.8 and 5.1 nm pores, the volume was divided, respectively, in five and six different regions. The boundaries of the various regions in the three pores are detailed in Table 3.

As mentioned above, the first monolayer of water molecules does not exhibit any translational mobility throughout the simulation, and so the diffusion coefficients shown in Table 1 for region 1 result from molecular displacements due to vibrations rather than from a true diffusive behavior. In the 1.3 nm pore, diffusion in the second monolayer is around 30% of the mobility observed for the molecules in the center of the pore (region 3). Still, in the central region, the diffusion coefficient of water ( $D_w$ ) is only about 1/3 of the bulk value. Comparison with data in wider pores indicates that this small



**Table 3. Boundaries of the Different Regions Defined for the Calculation of Diffusion Coefficients in the Three Titania Pores<sup>a</sup>**

region	$d = 1.3$ nm	$d = 2.8$ nm	$d = 5.1$ nm
1	$r > 5$	$r > 11.7$	$r > 23$
2	$2 < r < 5$	$8.9 < r < 11.7$	$23 < r < 20$
3	$r < 2$	$5.3 < r < 8.9$	$17 < r < 20$
4		$2.8 < r < 5.3$	$13 < r < 17$
5		$r < 2.8$	$10 < r < 13$
6			$r < 10$

<sup>a</sup>Regions 1, 2, and 3 have been defined in each pore to encompass the first, the second, and the third water layer, respectively. The entries represent the radius ( $r$ ) taken from the pore center, in Å.

value results from confinement rather than from the attractive potential of the surface. In fact, in the larger nanopores, the diffusion coefficients in the second and third layers are more than twice the  $D_w$  for the corresponding layers in the 1.3 nm pore. Interestingly, confinement seems to have little impact on diffusion coefficients for the two largest pores. Differences between the computed  $D_w$  values in the 2.8 and 5.1 nm pores are only minor. The variation of  $D_w$  and its different components as a function of the distance to the center of the pore, are shown in Figure 5 for all three systems. Not only are the behaviors in the two larger pores quite similar to each other, but they are in turn very close to the results reported for the planar titania–water interface in ref 56. The diffusivity increases rapidly reaching a plateau at approximately 10 Å from the walls

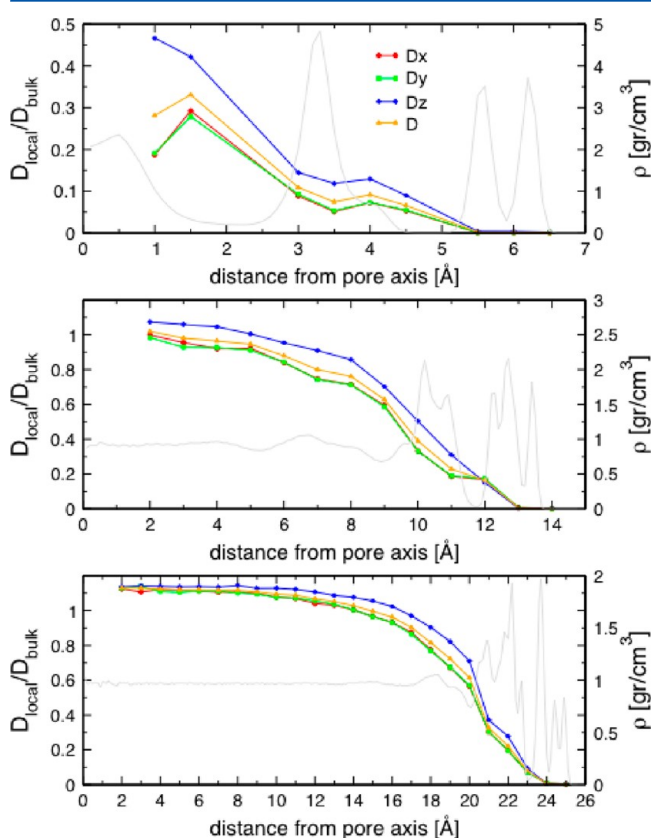


**Figure 5.** Diffusion coefficients as a function of the distance to the pore axis for the 1.3 (upper panel), 2.8 (middle panel), and 5.1 nm (lower panel) pores. Gray superimposed lines correspond to the radial density profile for each system.

in both pores, with  $D_w$  exhibiting comparable growth rates as a function of the separation from the surface. For a given layer the diffusion coefficient turns out to be smaller on the flat interface, simply because the multilayers are more compact in this geometry. The agreement across the two larger nanopores and the planar surface confirms that the observed decrease in diffusivity in the 2.8 and 5.1 nm pores results from the attractive potential at the interface, regardless of curvature or confinement. Noticeably, the diffusivity in the center of the 2.8 and 5.1 nm pores is slightly larger than in bulk. An analogous result has been already reported in simulations of water in silica pores of diameters between 2 and 4 nm by Milischuk and Ladanyi,<sup>44</sup> who attributed the enhanced diffusivity in the central region of the pores to the smaller density of the confined water. As will be seen in the next section, similar decreases in densities are measured in the present simulations, which also explain why  $D_w$  is marginally smaller in the 2.8 nm pore compared to the 5.1 nm pore. The diffusivity of water confined in cylindrical silica pores exhibits a similar increase in going from the interface to the center of the pore, but the bulk value is achieved at shorter separations, typically around 6–8 Å from the interface.<sup>39,44</sup> The survival probability function,  $P(t)$ , which measures the fraction of molecules that remain in the same region after an elapsed time, is plotted in Figure 6A for the first and the second hydration layers of the 1.3 and 2.8 nm pores. The decrease of  $P(t)$  becomes faster with the larger the diameter of the pore; the change in  $P(t)$  is large when going from the 1.3 nm to the 2.8 nm pore but becomes negligible between the two larger pores, consistently with the variation in the corresponding diffusivities. The residence time, which, in first order processes, can be defined according to how long it takes the fraction of molecules in some region to decay to  $1/e$ , for water in the first layer turns out to be of the order of several nanoseconds, exceeding the total simulation windows. These residence times are in agreement with those observed for slit  $\text{TiO}_2$  pores.<sup>36</sup> It is seen that the residence times drop 2 orders of magnitude already in the second layer, while in the third layer or beyond (results not shown), the residence times are indistinguishable from those corresponding to bulk water. It is also interesting to note that the residence times found for water in the second layer (around 10 ps) are comparable to the residence times informed for water in the first layer of less hydrophilic silica pores.<sup>44</sup> This finding supports the analogy between silica pores and titania pores of a larger diameter, discussed above. The dynamics of interfacial water has been studied on the basis of molecular simulations for various materials at the bulk–planar surface. Estimated residence times for  $\text{H}_2\text{O}$  molecules in the first hydration layer range from a few tens of picoseconds for silica<sup>44</sup> and mica,<sup>72</sup> to a few nanoseconds for oxides like  $\text{TiO}_2$  or  $\text{SnO}_2$ ,<sup>73</sup> or even more for alkali oxides such as  $\text{MgO}$ .<sup>74</sup> Residence times and diffusivities are also dependent on the degree of hydration. Figure 6B depicts the global diffusion coefficients of water as a function of the distance, for various fillings in the case of the larger pore; results in the other pores show the same trend. It can be seen that the diffusivity tends to decrease for higher fillings. Next to the outer shell (at the liquid–vacuum interface), the activation energy involved in the redistribution of bonds necessary for molecular diffusion is lower. In particular, in a thin adsorbed layer, the translational mobility will be less constrained than in a thick layer. This explains the steep rise in  $D_w$  found for fillings below 65%, where the condensed phase is still absent. The same behavior has been reported for partially filled silica nanopores.<sup>39</sup> Finally, Figure



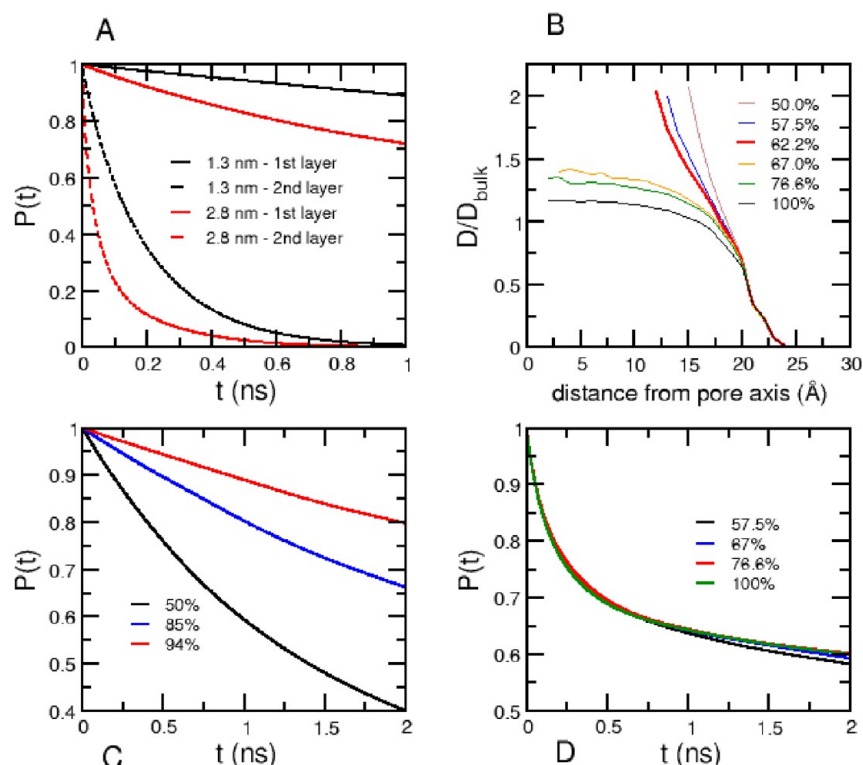


**Figure 6.** (A) Survival probability functions  $P(t)$  for molecules in the first and second hydration layers, in the 1.3 and 2.8 nm pores at maximum filling. (B) Total diffusion coefficient as a function of the distance, for the 5.1 nm pore at various fillings. (C)  $P(t)$  for the first hydration layer in the 1.3 nm pore at various fillings. (D)  $P(t)$  for the first hydration layer in the 5.1 nm pore at various fillings.

6C,D represents, respectively, the survival probability function for the molecules in the first layer, for the smaller and the larger pores. In the former, the residence times decrease in almost an order of magnitude when going from 94% to 50% filling. In the later, instead,  $P(t)$  is hardly sensitive to the hydration level in the range 57–100%. This can be understood noting that, in the 5 nm pore, beyond the formation of two fully adsorbed layers, which occurs for a filling of  $\sim 50\%$ , the addition of further water should not affect the dynamics of the molecules in the first layer.

The anisotropy in the diffusivity is only pronounced in the 1.3 nm pore (see Table 1 and Figure 5). In general, the diffusion coefficients tend to be larger in the  $z$ -direction, along which there is no confinement. A somehow surprising raise in the value of the perpendicular components of the diffusion coefficients is seen in the smallest pore at 1.5  $\text{\AA}$  from the center and, to a minor extent, also at around 4  $\text{\AA}$  for all the components of  $D_w$ . An explanation to this behavior may be found in noticing that these points coincide with the intermediate spaces between layers, where the probability of finding a molecule is very low, as evinced in the density profile of Figure 1, also shown in Figure 5. While water is highly stabilized within a layer, dwelling outside must be relatively unstable, meaning that any molecule in the intermediate region will be moving fast from one layer to the other. In the wider pores, differences between the components of  $D_w$  are never larger than 20% and disappear altogether when the fluid becomes homogeneous, at around 10  $\text{\AA}$  from the interface. Differences between the parallel and the perpendicular components of the diffusion coefficients have also turned out to be small in simulations of silica pores<sup>44</sup> and of the titania planar surface.<sup>56</sup>

As we have shown above for the translational dynamics, the rotational dynamics of confined water is also very much altered by the confining matrix. We summarize our findings for the three pores studied as well as for bulk water in Figure 7, which presents the dipole autocorrelation functions (eq 2). It is worth noting that the correlation functions presented in this figure contain the contributions of all water layers. Bulk water displays the fastest decay of the dipole autocorrelation function; the orientational correlations become slower with decreasing

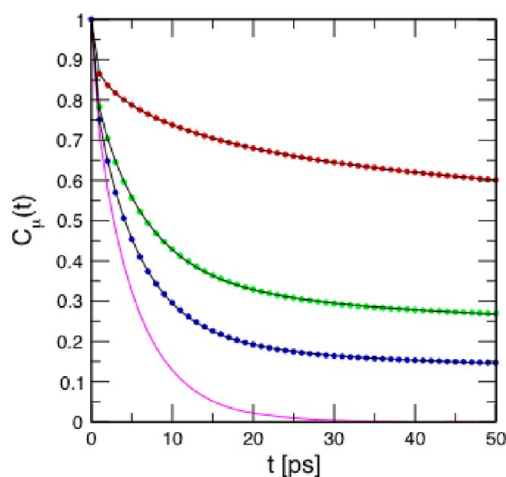


**Figure 7.** Single-dipole time correlation function for bulk (magenta line) and confined water (red circles = 1.3 nm pore at 94% filling; green circles = 2.8 nm pore at 100% filling; blue circles = 5.1 nm pore at 100% filling). Solid black lines correspond to the exponential fits (see eq 3).

diameter of the pore. It has been often found that the decay of  $C_\mu(t)$  in nanopores is well described by a linear combination of a simple and a stretched exponential:

$$C_\mu(t) \approx a_0 e^{-t/\tau_0} + a_1 e^{-(t/\tau_1)^\beta} \quad (3)$$

where the simple exponential term represents a decay with a short time scale, which may be ascribed to the contribution of faster molecules located away from the surface, while the stretched exponential represents slower relaxations that would arise from molecules closer to the surface.<sup>75–77</sup> Our data can be nicely fitted using this expression, with a short scale parameter ranging from 5.5 to 16.2 ps on decreasing the diameter of the pore (our computed orientational relaxation time for bulk water at 300 K and  $\rho = 1 \text{ g/cm}^3$  is 4.4 ps). Results of the fitting to eq 3 are shown in Table 4 and Figure 7. The coefficient  $\beta$  of the

**Table 4. Parameters for  $C_\mu(t)$  According to eq 3, Obtained for All Three Pores at 100% Filling<sup>a</sup>**

pore diameter (nm)	$a_0$	$\tau_0$ (ps)	$a_1$	$\tau_1$ (ps)	$\beta$	$R^2$
1.3	0.07	16.3	0.93	1000.0	0.27	0.999993
2.8	0.41	6.4	0.59	137.9	0.23	0.999996
5.1	0.57	5.6	0.43	34.4	0.22	0.999997

<sup>a</sup> $\tau_{\text{bulk}} = 4.4$  ps (computed from our MD simulation of bulk water at 300 K and  $\rho = 1 \text{ g/cm}^3$ , in agreement with literature values<sup>78</sup>).

stretched exponential is very low, around 0.2 for all pores, indicating widespread relaxation times in nanoconfined water. For the smaller pore, the contribution of fast relaxation is very small and the time scales very slow compared with those in bulk water, consistent with the almost immobilized water structure described above. For the 2.8 and 5.1 nm pores, the proportion of molecules contributing to the fast regime raises, and the fast relaxation times approach the bulk value, while those corresponding to the stretched exponential exhibit an important decrease. The observed confinement effects on the rotational dynamics must have a significant impact on the dielectric and optical responses of the confined water, the calculation of which (e.g., the static- and frequency-dependent permittivity) exceeds the scope of the present article and is the subject of ongoing work.

**Filling Mechanisms and Phase Transition.** In the Structure section, we have already discussed the filling of the 1.3 nm pore, which was observed to occur continuously, with no evidence of capillary condensation. In the 2.8 nm pore, the progressive addition of water molecules induces a homogeneous growth of the adsorbed phase, differently to what has been found for the narrower channel, where water tended to aggregate in small clusters upon completion of the first layer. The pronounced curvature of the 1.3 nm pore encourages the nucleation of these small clusters that maximize the water–water interactions, which seems unfeasible on a flatter surface. Figure 8 shows the surface density of water ( $\Gamma$ ) against the filling percentage for the three systems. Capillary condensation is detected in the 2.8 nm pore for a water content of 71%, when the fluid splits in two phases; i.e., a liquid plug in equilibrium with a surface adsorbed phase. With further filling, the densities of the liquid plug and the surface adsorbed phase remain constant, while the amount of each phase increases. Values in Figure 8 above the point of capillary condensation show the density of the surface adsorbed phase. It can be appreciated that the transition in the 2.8 nm pore takes place in equilibrium: as

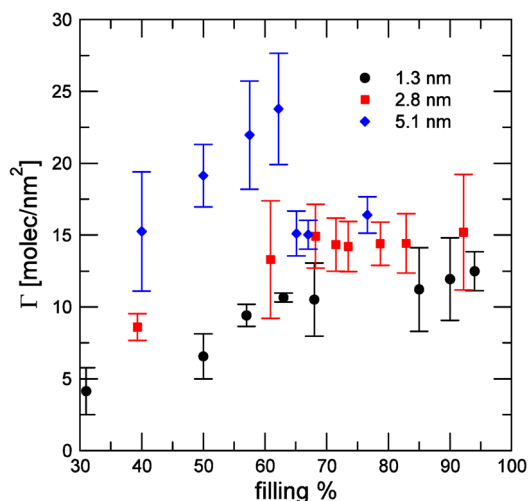


**Figure 8.** Density of the surface-adsorbed water phase as a function of filling percentage in the 1.3 (black circles), 2.8 (red squares), and 5.1 nm (blue diamonds) diameter pores. For fillings exhibiting phase coexistence, the density was calculated excluding the region occupied by the condensed phase.

soon as  $\Gamma$  reaches the equilibrium density  $\Gamma_{\text{eq}}$  (of around  $14 \text{ nm}^{-2}$ ), the condensed phase is formed. As stated in the Introduction, our previous investigations in less hydrophilic nanopores<sup>37,38</sup> showed that capillary condensation occurred in equilibrium conditions when the diameter was 1.5 nm and under strong supersaturation when it was 3 nm. In titania, the immobilized first layer causes a diminished effective radius, so that this pore of 2.8 nm can be comparable to one of around 2.0 nm exhibiting a less hydrophilic surface, for which adsorption hysteresis is still absent. We note that, if the density of the first monolayer (of around  $6 \text{ nm}^{-2}$ ) is subtracted from  $\Gamma_{\text{eq}}$ , a surface density of  $8 \text{ nm}^{-2}$  is recovered, comparable to the equilibrium value of  $\sim 6.5 \text{ nm}^{-2}$  found in the pores of moderate hydrophilicity.<sup>38</sup>

Figure 8 shows that  $\Gamma$  in the largest pore reaches a value of nearly  $25 \text{ nm}^{-2}$  just before capillary condensation, for a filling of 62%. Once the fluid condenses,  $\Gamma$  falls to an equilibrium value of around  $15 \text{ nm}^{-2}$ . This means that in the widest pore the transition is occurring out of equilibrium, probably accompanied by a pronounced hysteresis loop. The excess density necessary to unleash condensation, i.e., the difference between the saturation and the equilibrium densities, is  $10 \text{ nm}^{-2}$ . Comparison with the results for the 2.8 nm pore suggests that  $\Gamma_{\text{eq}}$  does not significantly depend on radius, as discussed elsewhere (see ref 38). Differently to what we had observed in the 2.8 nm pore and in other nanopores exhibiting capillary condensation,<sup>37,38</sup> in the 5.1 nm titania pore, the growth of the surface adsorbed phase turns out to be inhomogeneous after completion of the second monolayer. While the first and the second layers develop uniformly along the interface, for fillings above 40%, the water molecules start to accumulate in a certain region, resulting in a localized increment of the surface density that eventually leads to condensation. This behavior is depicted in Figure 9, which presents  $\Gamma$  along the pore axis for three different filling percentages: 40%, 62%, and 92%. These fillings correspond to points in the phase diagram before (40% and 62%) and after (92%) capillary condensation. We note that the strong oscillations in the axial density profile reflect the highly structured first layer, which adapts to the rutile surface; these oscillations are absent from the rest of the layers. For a content

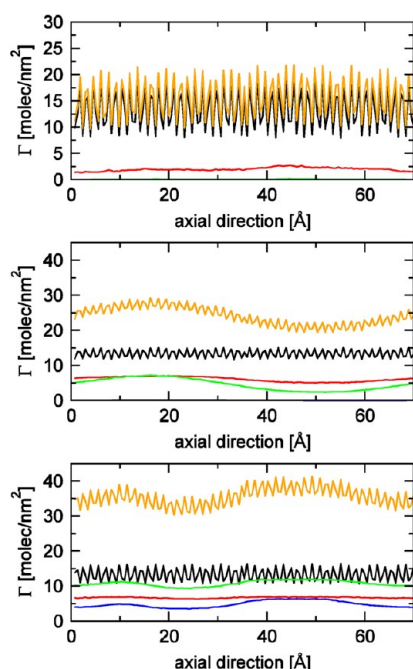


**Figure 9.** Axial density profiles of the 5.1 nm pore for 40% (upper panel), 62% (middle panel), and 92% fillings (lower panel). Orange lines corresponds to the total number of molecules per area, black lines to molecules with  $r > 20$  Å, red lines to molecules with  $20 > r > 17$  Å, green lines to molecules with  $17 > r > 10$  Å, and blue lines to molecules with  $r < 10$  Å. The fine, oscillatory structure appearing in the orange and black curves does not arise from nonconverged sampling, but from the immobilized water of the first hydration layer.

The above findings can be rationalized in the light of our previous results for water in hydrophilic and hydrophobic model nanopores.<sup>37,38</sup> In hydrophilic pores of up to 4 nm, we have shown that a surface adsorbed phase grows uniformly on the interface until condensation is observed. In a pore of 1.5 nm, the transition proceeds in equilibrium, whereas in 3 and 4 nm pores, capillary condensation requires an excess density above  $\Gamma_{eq}$  and is triggered by a density fluctuation that closes the gap between opposite sides of the channel, allowing for the nucleation of a liquid plug. Such an excess density depends strongly on radius, while it is practically independent of hydrophilicity.<sup>38</sup> In the present case, where the diameter is 5.1 nm, our simulations suggest that this density in excess distributes uniformly on the pore surface only up to a certain threshold, above which it collapses into an aggregate localized on one of the pore sides (see Figure 10). From this point, further filling causes the thickening of this aggregate, while  $\Gamma$  remains approximately constant anywhere else. The nucleation of a condensed phase becomes feasible when this aggregate is thick enough to close the gap in the pore, leading to capillary condensation with the sudden fall of the density of the surface adsorbed phase to  $\Gamma_{eq}$ .

Figure 11 is a cartoon of the three filling mechanisms discussed so far. Interestingly enough, the behaviors found for

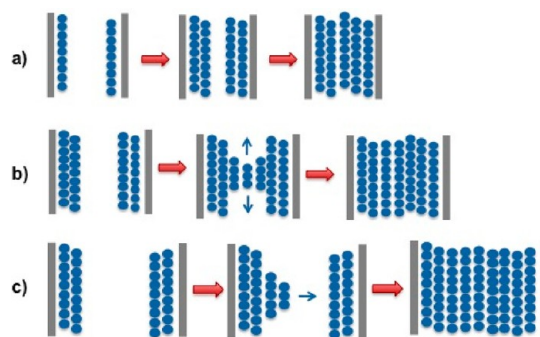


**Figure 11.** Filling mechanisms: (a) 1.3 nm pore, continuum growth, layer by layer on the pore walls, without the nucleation of a liquid plug; (b) 2.8 nm pore, axial growth, filling of the pore by capillary condensation; (c) 5.1 nm pore, radial growth.

the 2.8 and 5.1 nm pores can be identified, respectively, with the filling mechanisms proposed for silica pores of 3.3 and 8 nm by Grünberg and co-authors<sup>21</sup> (Figure 11B,C). The occurrence of one or the other mechanism is determined by pore radius in the first place and, to a lesser extent, by hydrophilicity. In fact, the radial thickening of a water aggregate in the 5.1 nm titania pore resembles the hydrophobic transition characterized in 3.0 and 4.0 nm nanopores with adsorption energies below 7 kcal/mol.<sup>38</sup> It is apparent, then, that a hydrophilic surface favors the stabilization of a homogeneous water coverage, even in conditions of supersaturation. For titania, the water is distributed uniformly up to a surface coverage of approximately  $15 \text{ nm}^{-2}$ . For a diameter of 5.1 nm, this excess density is still insufficient to induce capillary condensation. Above a surface density of  $15 \text{ nm}^{-2}$ , the development of additional homogeneous layers becomes unstable against the formation of a water aggregate, which growth would at last lead to capillary condensation.

For water fillings higher than 71% and 65%, respectively, in the 2.8 and 5.1 nm pores, a surface adsorbed phase coexists with a condensed fluid. This latter phase represents the

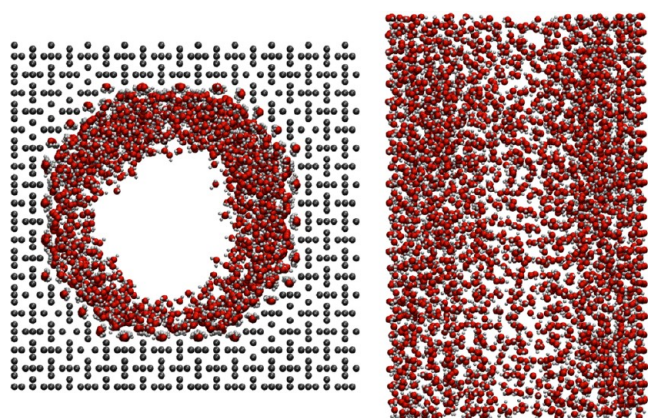


**Figure 10.** Snapshots of the 5.1 nm pore at 62% filling, front (left) and axial (right) views, in which pore atoms were hidden to facilitate the visualization of the water. Red corresponds to oxygen atoms, white to hydrogen atoms, and gray to the pore atoms.



confined liquid in equilibrium at the pressure of capillary condensation. Thus, properties such as the diffusion coefficient (presented in Table 1 and Figure 5) and the density of confined liquid water can be extracted from canonical molecular dynamics, instead of resorting to grand canonical Monte Carlo simulation, which is the usual approach to compute these properties at a fixed pressure. Then, the water density in the pores at a hundred percent filling was estimated from these phases, by averaging the number of H<sub>2</sub>O molecules inside a cylindrical volume in the central region of the channel (defined by  $r < 2.8$  Å in the pore of 2.8 nm and by  $r < 10$  Å in the pore of 5.1 nm) where the density is seen to be uniform. The densities calculated in this way turn out to be 0.93 and 0.96 g/cm<sup>3</sup> for the 2.8 and 5.1 nm pores, respectively. Experiments by Jähnert et al. in cylindrical silica pores of diameters between 2.5 and 4.4 nm revealed a 7% decrease in the density of confined water.<sup>18</sup> It should be noticed, though, that these measurements correspond to an average density of the liquid phase filling the nanopore (which exhibits strong fluctuations near the walls), while the values presented here were collected at the center of each pore, where the properties of the liquid are homogeneous.

## FINAL REMARKS

Water is tightly bound at the interface of titania nanopores, conforming a first compact monolayer, which, to all practical effects, can not be considered to be part of the fluid phase. As a consequence, the effective or accessible diameter of TiO<sub>2</sub> nanopores is around 0.6 nm smaller than the physical diameter. In this way, and concerning water properties, titania pores would behave similarly to pores of less hydrophilic materials (like silica) of slightly smaller radius. The simulations reveal that properties like the density and the diffusivity are significantly affected near the interface, plateauing at around 10 Å from the walls. In silica, these properties have been seen to plateau much faster, typically at 5 Å from the interface (see, for example, refs 39 and 44).

Capillary condensation in titania pores of 2.8 nm occurs in equilibrium. For a pore of 5.1 nm, instead, condensation may only take place under conditions of supersaturation, which implies an excess density of water molecules close to 10 nm<sup>-2</sup>. In titania pores, such an excess density distributes homogeneously until  $\Gamma$  reaches a value of approximately 15 nm<sup>-2</sup>. Beyond this amount, the water molecules aggregate forming a cluster in a localized region of the pore, which grows radially and axially until a plug develops. More generally, the following conclusions can be outlined: (i) capillary condensation in pores larger than ~2 nm (of effective diameter) requires the presence of an excess density, whose precise value is essentially determined by the diameter of the pore; (ii) the organization of this excess density depends on the surface affinity for water: in moderately hydrophobic pores there is a localized growth of surface density  $\Gamma$ , while in hydrophilic pores, the water tends to distribute homogeneously; (iii) if the pore is wide enough, the growth of uniform layers will eventually collapse to a localized distribution in equilibrium with a homogeneous adsorbed phase before capillary condensation takes place.

In a previous study,<sup>38</sup> we stated that, for a given pore size, the excess density (needed to produce condensation) first increases with hydrophilicity but soon tends to plateau because, as the surface is totally covered with H<sub>2</sub>O, the fluid becomes insensitive to the nature of the solid. This is true for surfaces of relatively high water affinity (adsorption energies of up to 15 kcal/mol); however, for an extremely hydrophilic interface as

the present one, a new effect comes into the scene: the immobilization of the water molecules on the surface, which leads to a decrease in the effective radius of the pore.

The visualization of the several aspects presented in this work is important for understanding the geometry and topology of water within the mesopores, which is determinant of chemical potential. This is an indeed relevant issue for sought applications in photocatalysis, solar cells, perm-selective membranes, and optical materials.

## ASSOCIATED CONTENT

### Supporting Information

Figures giving information on the pore crystallographic axis and details on the filling of the 1.3 and 2.8 nm pores. This material is available free of charge via the Internet at <http://pubs.acs.org>.

## AUTHOR INFORMATION

### Corresponding Author

\*E-mail: [damian@qi.fcen.uba.ar](mailto:damian@qi.fcen.uba.ar).

### Notes

The authors declare no competing financial interest.

## ACKNOWLEDGMENTS

This work has been supported by the Agencia Nacional de Promoción Científica y Tecnológica de Argentina through collaborative research grant PICT 2007-2111 (to V.M. and D.A.S.) and PICT 1848 (to G.S.I.). E.G.S. and E.dL. acknowledge CONICET for doctoral fellowships. We thank the Center of High Performance Computing at the University of Utah for allocation of computer time.

## REFERENCES

- (1) Mann, S.; Ozin, G. A. Synthesis of Inorganic Materials with Complex Form. *Nature* **1996**, *382*, 313–318.
- (2) Alfredsson, V.; Anderson, M. W. Structure of MCM-48 Revealed by Transmission Electron Microscopy. *Chem. Mater.* **1996**, *8*, 1141–1146.
- (3) Wong, M. S.; Jeng, E. S.; Ying, J. Y. Supramolecular Templating of Thermally Stable Crystalline Mesoporous Metal Oxides Using Nanoparticulate Precursors. *Nano Lett.* **2001**, *1*, 637–642.
- (4) Luo, H.; Wang, C.; Yan, Y. Synthesis of Mesoporous Titania with Controlled Crystalline Framework. *Chem. Mater.* **2003**, *15*, 3841–3846.
- (5) Soler-Illia, G. J. de A. A.; Sanchez, C.; Lebeau, B.; Patarin, J. Chemical Strategies To Design Textured Materials: from Microporous and Mesoporous Oxides to Nanonetworks and Hierarchical Structures. *Chem. Rev.* **2002**, *102*, 4093–4138.
- (6) Tian, B.; Liu, X.; Solovyov, L. A.; Liu, Z.; Yang, H.; Zhang, Z.; Xie, S.; Zhang, F.; Tu, B.; Yu, C.; Terasaki, O.; Zhao, D. Facile Synthesis and Characterization of Novel Mesoporous and Mesorelief Oxides with Gyroidal Structures. *J. Am. Chem. Soc.* **2003**, *126*, 865–875.
- (7) Wan, Y.; Dongyuan. On the Controllable Soft-Templating Approach to Mesoporous Silicates. *Chem. Rev.* **2007**, *107*, 2821–2860.
- (8) Lee, J.; Christopher Orilall, M.; Warren, S. C.; Kamperman, M.; DiSalvo, F. J.; Wiesner, U. Direct Access to Thermally Stable and Highly Crystalline Mesoporous Transition-Metal Oxides with Uniform Pores. *Nat. Mater.* **2008**, *7*, 222–228.
- (9) Jaroniec; Schüth, F. Preface to the Special Issue: Templated Materials. *Chem. Mater.* **2008**, *20*, 599–600.
- (10) Rozes, L.; Sanchez, C. Titanium Oxo-Clusters: Precursors for a Lego-Like Construction of Nanostructured Hybrid Materials. *Chem. Soc. Rev.* **2011**, *40*, 1006–1030.

- (11) Llewellyn, P. L.; Schueth, F.; Grillet, Y.; Rouquerol, F.; Rouquerol, J.; Unger, K. K. Water Sorption on Mesoporous Aluminosilicate MCM-41. *Langmuir* **1995**, *11*, 574–577.
- (12) Branton, P. J.; Hall, P. G.; Treguer, M.; Sing, K. S. W. Adsorption of Carbon Dioxide, Sulfur Dioxide and Water Vapour by MCM-41 a Model Mesoporous Adsorbent. *J. Chem. Soc., Faraday Trans.* **1995**, *91*, 2041–2043.
- (13) Inagaki, S.; Fukushima, Y. Adsorption of Water Vapor and Hydrophobicity of Ordered Mesoporous Silica, FSM-16. *Microporous Mesoporous Mater.* **1998**, *21*, 667–672.
- (14) Oh, J. S.; Shim, W. G.; Lee, J. W.; Kim, J. H.; Moon, H.; Seo, G. Adsorption Equilibrium of Water Vapor on Mesoporous Materials. *J. Chem. Eng. Data* **2003**, *48*, 1458–1462.
- (15) Ng, E.-P.; Mintova, S. Nanoporous Materials with Enhanced Hydrophilicity and High Water Sorption Capacity. *Microporous Mesoporous Mater.* **2008**, *114*, 1–26.
- (16) Kocherbitov, V.; Alfredsson, V. Assessment of Porosities of SBA-15 and MCM-41 Using Water Sorption Calorimetry. *Langmuir* **2011**, *27*, 3889–3897.
- (17) Morishige, K.; Uematsu, H. The Proper Structure of Cubic Ice Confined in Mesopores. *J. Chem. Phys.* **2005**, *122*, 044711–044711–4.
- (18) Chen, S.-H.; Mallamace, F.; Mou, C.-Y.; Broccio, M.; Corsaro, C.; Faraone, A.; Liu, L. The Violation of the Stokes–Einstein Relation in Supercooled Water. *Proc. Natl. Acad. Sci.* **2006**, *103*, 12974–12978.
- (19) Jaehnert, S.; Chavez, F. V.; Schaumann, G. E.; Schreiber, A.; Schoenhoff, M.; Findenegg, G. H. Melting and Freezing of Water in Cylindrical Silica Nanopores RID E-6935-2011. *Phys. Chem. Chem. Phys.* **2008**, *10*, 6039–6051.
- (20) Erko, M.; Findenegg, G. H.; Cade, N.; Michette, A. G.; Paris, O. Confinement-Induced Structural Changes of Water Studied by Raman Scattering. *Phys. Rev. B* **2011**, *84*, 104205.
- (21) Grünberg, B.; Emmeler, T.; Gedat, E.; Shenderovich, I.; Findenegg, G. H.; Limbach, H.; Buntkowsky, G. Hydrogen Bonding of Water Confined in Mesoporous Silica MCM-41 and SBA-15 Studied by <sup>1</sup>H Solid-State NMR. *Chem.—Eur. J.* **2004**, *10*, 5689–5696.
- (22) Schoch, R. B.; Han, J.; Renaud, P. Transport Phenomena in Nanofluidics. *Rev. Mod. Phys.* **2008**, *80*, 839–883.
- (23) Takahara, S.; Nakano, M.; Kittaka, S.; Kuroda, Y.; Mori, T.; Hamano, H.; Yamaguchi, T. Neutron Scattering Study on Dynamics of Water Molecules in MCM-41. *J. Phys. Chem. B* **1999**, *103*, 5814–5819.
- (24) Takahara, S.; Sumiyama, N.; Kittaka, S.; Yamaguchi, T.; Bellissent-Funel, M.-C. Neutron Scattering Study on Dynamics of Water Molecules in MCM-41. 2. Determination of Translational Diffusion Coefficient. *J. Phys. Chem. B* **2005**, *109*, 11231–11239.
- (25) Steiner, E.; Bouguet-Bonnet, S.; Blin, J.-L.; Canet, D. Water Behavior in Mesoporous Materials As Studied by NMR Relaxometry. *J. Phys. Chem. A* **2011**, *115*, 9941–9946.
- (26) Papadopolou, A.; Van Swol, F.; Marini Bettolo Marconi, U. Pore-End Effects on Adsorption Hysteresis in Cylindrical and Slitlike Pores. *J. Chem. Phys.* **1992**, *97*, 6942–6952.
- (27) Heffelfinger, G. S.; Van Swol, F.; Gubbins, K. E. Adsorption Hysteresis in Narrow Pores. *J. Chem. Phys.* **1988**, *89*, 5202–5205.
- (28) Vishnyakov, A.; Neimark, A. V. Studies of Liquid–Vapor Equilibria, Criticality, and Spinodal Transitions in Nanopores by the Gauge Cell Monte Carlo Simulation Method. *J. Phys. Chem. B* **2001**, *105*, 7009–7020.
- (29) Brovchenko, I.; Geiger, A.; Oleinikova, A.; Paschek, D. Phase Coexistence and Dynamic Properties of Water in Nanopores. *Eur. Phys. J. E* **2003**, *12*, 69–76.
- (30) Brovchenko, I.; Geiger, A.; Oleinikova, A. Water in Nanopores. I. Coexistence Curves from Gibbs Ensemble Monte Carlo Simulations. *J. Chem. Phys.* **2004**, *120*, 1958–1972.
- (31) Kierlik, E.; Puibasset, J.; Tarjus, G. Effect of the Reservoir Size on Gas Adsorption in Inhomogeneous Porous Media. *J. Phys.: Condens. Matter* **2009**, *21*, 155102.
- (32) Smit, B.; Maesen, T. L. M. Molecular Simulations of Zeolites: Adsorption, Diffusion, and Shape Selectivity. *Chem. Rev.* **2008**, *108*, 4125–4184.
- (33) Giovambattista, N.; Rossky, P. J.; Debenedetti, P. G. Effect of Temperature on the Structure and Phase Behavior of Water Confined by Hydrophobic, Hydrophilic, and Heterogeneous Surfaces. *J. Phys. Chem. B* **2009**, *113*, 13723–13734.
- (34) Romero-Vargas Castrillón, S.; Giovambattista, N.; Aksay, I. A.; Debenedetti, P. G. Effect of Surface Polarity on the Structure and Dynamics of Water in Nanoscale Confinement. *J. Phys. Chem. B* **2009**, *113*, 1438–1446.
- (35) Romero-Vargas Castrillón, S.; Giovambattista, N.; Aksay, I. A.; Debenedetti, P. G. Evolution from Surface-Influenced to Bulk-Like Dynamics in Nanoscopically Confined Water. *J. Phys. Chem. B* **2009**, *113*, 7973–7976.
- (36) Wei, M.-J.; Zhou, J.; Lu, X.; Zhu, Y.; Liu, W.; Lu, L.; Zhang, L. Diffusion of Water Molecules Confined in Slits of Rutile TiO<sub>2</sub>(110) and graphite(0001). *Fluid Phase Equilib.* **2011**, *302*, 316–320.
- (37) De la Llave, E.; Molinero, V.; Scherlis, D. A. Water Filling of Hydrophilic Nanopores. *J. Chem. Phys.* **2010**, *133*, 034513.
- (38) De la Llave, E.; Molinero, V.; Scherlis, D. A. *J. Phys. Chem. C* **2012**, *116*, 1833–1840.
- (39) Shirono, K.; Daiguji, H. Molecular Simulation of the Phase Behavior of Water Confined in Silica Nanopores. *J. Phys. Chem. C* **2007**, *111*, 7938–7946.
- (40) Malani, A.; Ayappa, K. G.; Murad, S. Influence of Hydrophilic Surface Specificity on the Structural Properties of Confined Water. *J. Phys. Chem. B* **2009**, *113*, 13825–13839.
- (41) Gallo, P.; Rovere, M.; Spohr, E. Glass Transition and Layering Effects in Confined Water: A Computer Simulation Study. *J. Chem. Phys.* **2000**, *113*, 11324–11335.
- (42) Gallo, P.; Rapinesi, M.; Rovere, M. Confined Water in the Low Hydration Regime. *J. Chem. Phys.* **2002**, *117*, 369–375.
- (43) Gallo, P.; Rovere, M.; Chen, S.-H. Dynamic Crossover in Supercooled Confined Water: Understanding Bulk Properties through Confinement. *J. Phys. Chem. Lett.* **2010**, *1*, 729–733.
- (44) Milischuk, A. A.; Ladanyi, B. M. Structure and Dynamics of Water Confined in Silica Nanopores. *J. Chem. Phys.* **2011**, *135*, 174709.
- (45) Chen, X.; Mao, S. S. Titanium Dioxide Nanomaterials: Synthesis, Properties, Modifications, and Applications. *Chem. Rev.* **2007**, *107*, 2891–2959.
- (46) Soler-Illia, G. J. A. A.; Angelomé, P. C.; Fuentès, M. C.; Grosso, D.; Boissière, C. Critical Aspects in the Production of Periodically Ordered Mesoporous Titania Thin Films. *Nanoscale* **2012**, *4*, 2549–2566.
- (47) Zhang, C.; Lindan, P. J. D. Multilayer Water Adsorption on Rutile TiO<sub>2</sub>(110): A First-Principles Study. *J. Chem. Phys.* **2003**, *118*, 4620.
- (48) Harris, L. A.; Quong, A. A. Molecular Chemisorption As the Theoretically Preferred Pathway for Water Adsorption on Ideal Rutile TiO<sub>2</sub>(110). *Phys. Rev. Lett.* **2004**, *93*, 086105.
- (49) Tilocca, A.; Selloni, A. Vertical and Lateral Order in Adsorbed Water Layers on Anatase TiO<sub>2</sub>(101). *Langmuir* **2004**, *20*, 8379–8384.
- (50) Bandura, A. V.; Kubicki, J. D.; Sofo, J. O. Comparisons of Multilayer H<sub>2</sub>O Adsorption onto the (110) Surfaces of  $\alpha$ -TiO<sub>2</sub> and SnO<sub>2</sub> As Calculated with Density Functional Theory. *J. Phys. Chem. B* **2008**, *112*, 11616–11624.
- (51) Kowalski, P. M.; Meyer, B.; Marx, D. Composition, Structure, and Stability of the Rutile TiO<sub>2</sub>(110) Surface: Oxygen Depletion, Hydroxylation, Hydrogen Migration, and Water Adsorption. *Phys. Rev. B* **2009**, *79*, 115410.
- (52) Sánchez, V. M.; De la Llave, E.; Scherlis, D. A. Adsorption of R–OH Molecules on TiO<sub>2</sub> Surfaces at the Solid–Liquid Interface. *Langmuir* **2011**, *27*, 2411–2419.
- (53) Sun, C.; Liu, L.-M.; Selloni, A.; Lu, G. Q.; Smith, S. C. Titania–Water Interactions: A Review of Theoretical Studies. *J. Mater. Chem.* **2010**, *20*, 10319–10334.
- (54) Bandura, A. V.; Kubicki, J. D. Derivation of Force Field Parameters for TiO<sub>2</sub>–H<sub>2</sub>O Systems from ab Initio Calculations. *J. Phys. Chem. B* **2003**, *107*, 11072–11081.

- (55) Alimohammadi, M.; Fichthorn, K. A. A Force Field for the Interaction of Water with TiO<sub>2</sub> Surfaces. *J. Phys. Chem. C* **2011**, *115*, 24206–24214.
- (56) Předota, M.; Bandura, A. V.; Cummings, P. T.; Kubicki, J. D.; Wesolowski, D. J.; Chialvo, A. A.; Machesky, M. L. Electric Double Layer at the Rutile (110) Surface. 1. Structure of Surfaces and Interfacial Water from Molecular Dynamics by Use of ab Initio Potentials. *J. Phys. Chem. B* **2004**, *108*, 12049–12060.
- (57) Koparde, V. N.; Cummings, P. T. Molecular Dynamics Study of Water Adsorption on TiO<sub>2</sub> Nanoparticles. *J. Phys. Chem. C* **2007**, *111*, 6920–6926.
- (58) De la Llave, E. Modelado Computacional del Comportamiento Molecular en Interfases y Entornos Nanoestructurados. Ph.D. thesis, Universidad de Buenos Aires, 2012.
- (59) Berendsen, H. J. C.; Grigera, J. R.; Straatsma, T. P. The Missing Term in Effective Pair Potentials. *J. Phys. Chem.* **1987**, *91*, 6269–6271.
- (60) Ryckaert, J.-P.; Cicciotti, G.; Berendsen, H. J. C. Numerical Integration of the Cartesian Equations of Motion of a System with Constraints: Molecular Dynamics of *n*-Alkanes. *J. Comput. Phys.* **1977**, *23*, 327–341.
- (61) Masanori, M.; Akaogi, M. Molecular Dynamics Simulation of the Structural and Physical Properties of the Four Polymorphs of TiO<sub>2</sub>. *Mol. Simul.* **1991**, *6*, 239–244.
- (62) Plimpton, S. Fast Parallel Algorithms for Short-Range Molecular Dynamics. *J. Comput. Phys.* **1995**, *117*, 1–19.
- (63) LAMMPS Molecular Dynamics Simulator. <http://lammps.sandia.gov>.
- (64) Hockney, R. W.; Eastwood, J. W. *Computer Simulation Using Particles*; Taylor & Francis: New York, 1992.
- (65) Humphrey, W.; Dalke, A.; Schulten, K. VMD: Visual Molecular Dynamics. *J. Mol. Graphics* **1996**, *14*, 33–38.
- (66) Lounnas, V.; Pettitt, B. M.; Phillips, G. N. A Global Model of the Protein–Solvent Interface. *Biophys. J.* **1994**, *66*, 601–614.
- (67) Lee, S. L.; DeBenedetti, P. G.; Errington, J. R. A Computational Study of Hydration, Solution Structure, and Dynamics in Dilute Carbohydrate Solutions. *J. Chem. Phys.* **2005**, *122*, 204511–204511–10.
- (68) Naono, H.; Hakuman, M. Analysis of Porous Texture by Means of Water Vapor Adsorption Isotherm with Particular Attention to Lower Limit of Hysteresis Loop. *J. Colloid Interface Sci.* **1993**, *158*, 19–26.
- (69) Předota, M.; Cummings, P. T.; Wesolowski, D. J. Electric Double Layer at the Rutile (110) Surface. 3. Inhomogeneous Viscosity and Diffusivity Measurement by Computer Simulations. *J. Phys. Chem. C* **2007**, *111*, 3071–3079.
- (70) Mamontov, E.; Wesolowski, D. J.; Vlcek, L.; Cummings, P. T.; Rosenqvist, J.; Wang, W.; Cole, D. R. Dynamics of Hydration Water on Rutile Studied by Backscattering Neutron Spectroscopy and Molecular Dynamics Simulation. *J. Phys. Chem. C* **2008**, *112*, 12334–12341.
- (71) Mancinelli, R.; Imberti, S.; Soper, A. K.; Liu, K. H.; Mou, C. Y.; Bruni, F.; Ricci, M. A. Multiscale Approach to the Structural Study of Water Confined in MCM41. *J. Phys. Chem. B* **2009**, *113*, 16169–16177.
- (72) Sakuma, H.; Kawamura, K. Structure and Dynamics of Water on Li<sup>+</sup>, Na<sup>+</sup>, K<sup>+</sup>, Cs<sup>+</sup>, H<sub>3</sub>O<sup>+</sup>-Exchanged Muscovite Surfaces: A Molecular Dynamics Study. *Geochim. Cosmochim. Acta* **2011**, *75*, 63–81.
- (73) Mamontov, E.; Vlcek, L.; Wesolowski, D. J.; Cummings, P. T.; Wang, W.; Anovitz, L. M.; Rosenqvist, J.; Brown, C. M.; Garcia Sakai, V. Dynamics and Structure of Hydration Water on Rutile and Cassiterite Nanopowders Studied by Quasielastic Neutron Scattering and Molecular Dynamics Simulations. *J. Phys. Chem. C* **2007**, *111*, 4328–4341.
- (74) Deshmukh, S. A.; Sankaranarayanan, S. K. R. S. Atomic Scale Characterization of Interfacial Water near an Oxide Surface Using Molecular Dynamics Simulations. *Phys. Chem. Chem. Phys.* **2012**, *14*, 15593–15605.
- (75) Sciortino, F.; Gallo, P.; Tartaglia, P.; Chen, S.-H. Supercooled Water and the Kinetic Glass Transition. *Phys. Rev. E* **1996**, *54*, 6331–6343.
- (76) Farrer, R. A.; Fourkas, J. T. Orientational Dynamics of Liquids Confined in Nanoporous Sol–Gel Glasses Studied by Optical Kerr Effect Spectroscopy. *Acc. Chem. Res.* **2003**, *36*, 605–612.
- (77) Elola, M. D.; Rodriguez, J.; Laria, D. Structure and Dynamics of Liquid Methanol Confined within Functionalized Silica Nanopores. *J. Chem. Phys.* **2010**, *133*, 154707–154707–9.
- (78) Van der Spoel, D.; Van Maaren, P. J.; Berendsen, H. J. C. A Systematic Study of Water Models for Molecular Simulation: Derivation of Water Models Optimized for Use with a Reaction Field. *J. Chem. Phys.* **1998**, *108*, 10220–10230.
- (79) Luzar, A.; Chandler, D. Structure and Hydrogen Bond Dynamics of Water–Dimethyl Sulfoxide Mixtures by Computer Simulations. *J. Chem. Phys.* **1993**, *98*, 8160.